Nano Research

Open Access

Research Article

Zoledronate-loaded aluminum salt nanovaccines amplify cellular immune response by enhancing cross-presentation

Chunting He[§], Penghui He[§], Xue Tang, Shuting Bai, Ming Qin, Yunting Zhang, Zhaofei Guo, Guangsheng Du, and Xun Sun ✉

Key Laboratory of Drug-Targeting and Drug Delivery System of the Education Ministry, West China School of Pharmacy, Sichuan University, Chengdu 610041, China

[§] *Chunting He and Penghui He contributed equally to this work.*

Cite this article: *Nano Research*, **2025**, *18*, 94907010. https://doi.org/10.26599/NR.2025.94907010

ABSTRACT: Being a Th2 stimulator, classic aluminum salt-based adjuvants only stimulate weak cellular immune responses that are required for vaccination against intracellular viruses or cancerous cells. As a third-generation bisphosphonate, zoledronate (ZOL) can enhance antigen cross-presentation by inhibiting key enzymes of the mevalonate pathway. Here, we developed the subunit antigen ovalbumin (OVA) and ZOL co-loaded aluminum hydroxide nanoparticles (APN-OVA-ZOL) and investigated their capacity for inducing cellular immune responses against the antigen. Our results showed that the developed nanovaccines could successfully encapsulate OVA and ZOL, and enabled efficient lymph node delivery. Benefited by the mevalonate pathway inhibition effect of ZOL, APN-OVA-ZOL significantly promoted cross-presentation. As a result, APN-OVA-ZOL induced robust cellular immunity, including the activation of T and B cells. In a EG7-OVA tumor-bearing murine model, APN-OVA-ZOL significantly inhibited the tumor growth and prolonged mice survival. This work provided a strong empirical foundation indicating that zoledronate-loaded aluminum salt nanovaccines had a strong potency for cancer immunotherapy.

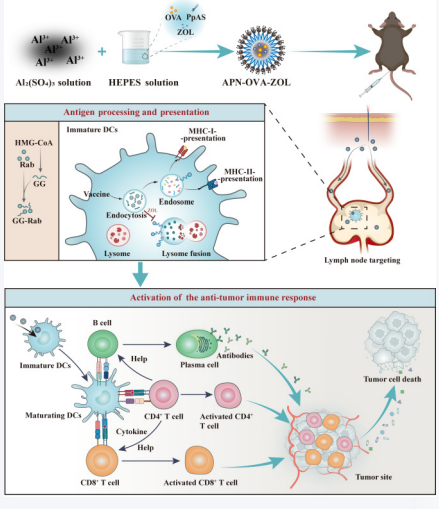

KEYWORDS: zoledronate (ZOL), mevalonate pathway, antigen cross-presentation, cellular immune responses

1 Introduction

With the theoretical and technological revolutions in immunology, the applications of vaccines have expanded from the prevention of infectious diseases to treating cancer and inflammation-related diseases. Compared with the traditional attenuated or inactivated pathogen-based vaccines, subunit vaccines have received increasing attention due to their high safety and easiness of mass production. The subunit vaccine exploits pathogen subunits as antigens, e.g., recombinant proteins or synthetic peptides, allowing for highly specific immune responses against the pathogens. However, subunit antigens usually have poor immunogenicity, and mostly often a potent adjuvant or delivery system need to be used to ensure robust immune responses. On the other hand, only several adjuvants have been licensed for human use, and they mainly stimulate antibody-mediated humoral immunity but can only elicit poor cellular immune responses, which are critical for vaccination against intracellular viruses or cancerous cells [1, 2]. In sum, the development of safe and effective adjuvant systems that can stimulate potent cellular immunity remains a major challenge for subunit vaccines [3].

Efficient antigen cross-presentation and T cell activation are critical for subunit vaccines to induce potent cellular immunity, particularly $CD8^+$ T cell immune response. The activated $CD8^+$ T lymphocytes further develop to cytotoxic T lymphocytes (CTLs), which can directly eliminate virus-infected cells or cancer cells [4–6]. Previous studies have shown that interstitially injected nanovaccines with a diameter of 10–100 nm can efficiently drain to the lymph nodes by penetrating the gaps among lymphoepithelial cells [7, 8]. As a result, these nanovaccines could induce effective cross-presentation, as the lymph nodes harbor large amounts of specialized $CD8\alpha^+$ dendritic cell (DC) subsets that are capable of priming CTL responses via the cross-presentation [9, 10].

Received: June 18, 2024; **Revised:** August 22, 2024
Accepted: August 28, 2024

✉Address correspondence to sunxun@scu.edu.cn

This mechanism provides a theoretical basis for the construction of lymph node-targeting delivery vectors. Under this context, an increasing number of nanocarriers that have superior lymph-node targeting capacity have been developed for vaccine delivery, including liposomes, polymeric nanocarriers, biomimetic nanocarriers, and inorganic nanocarriers (e.g. mesoporous silica nanoparticles, gold nanoparticles, calcium phosphate nanoparticles) [11–13]. However, the clinical application of these nano vaccines is limited due to their potential safety concerns brought by the non-FDA-approved carrier materials or additional adjuvants. In our group, we have previously fabricated aluminum hydroxide-based nanovaccines [14], which could incorporate both the antigen and Toll-like receptor 9 (TLR9) agonist cytosine phosphate guanine (CpG). As compared to FDA-approved traditional alum adjuvant, our developed aluminum hydroxide nanocarriers not only can efficiently load antigen/adjuvant through electrostatic interaction, but also stimulate potent cellular immunity due to the lymph node targeted co-delivery of the antigen and adjuvant [15]. The ability of CpG to induce a Th1-biased and $CD8^+$ T-cell response in preclinical studies suggests they might be promising adjuvants for cancer vaccines. Still, some issues remain, such as the existence of significant species specificity of CpG oligodeoxynucleotide (CpG ODN), the uncertainty of the optimal immunization dose and safety, the complex synthesis process and quality control [16, 17].

As a third-generation bisphosphonate, zoledronate is one of the most widely used drugs for osteoporosis in the clinic. Previous studies have also shown that zoledronate (ZOL) can inhibit the mevalonate pathway that affected the process of endosome-lysosome fusion process [18, 19]. As a result, zoledronate can help to slow down the acidification of dendritic cells and the maturation of phagosomes, thereby facilitating cross-presentation for triggering a powerful T-cell immune response [20]. However, due to its poor membrane permeability, zoledronate could be easily eliminated by local tissues, making it difficult to maximize its immunomodulatory effect. It is necessary to construct an appropriate vaccine vector to improve the delivery efficiency of zoledronate.

In current study (Fig. 1), we constructed a zoledronate-loaded aluminum hydroxide nanovaccines to amplify $CD8^+$ T cell responses against a subunit protein antigen. Specifically, we modified aluminum hydroxide with a wheat-shaped polyethylene

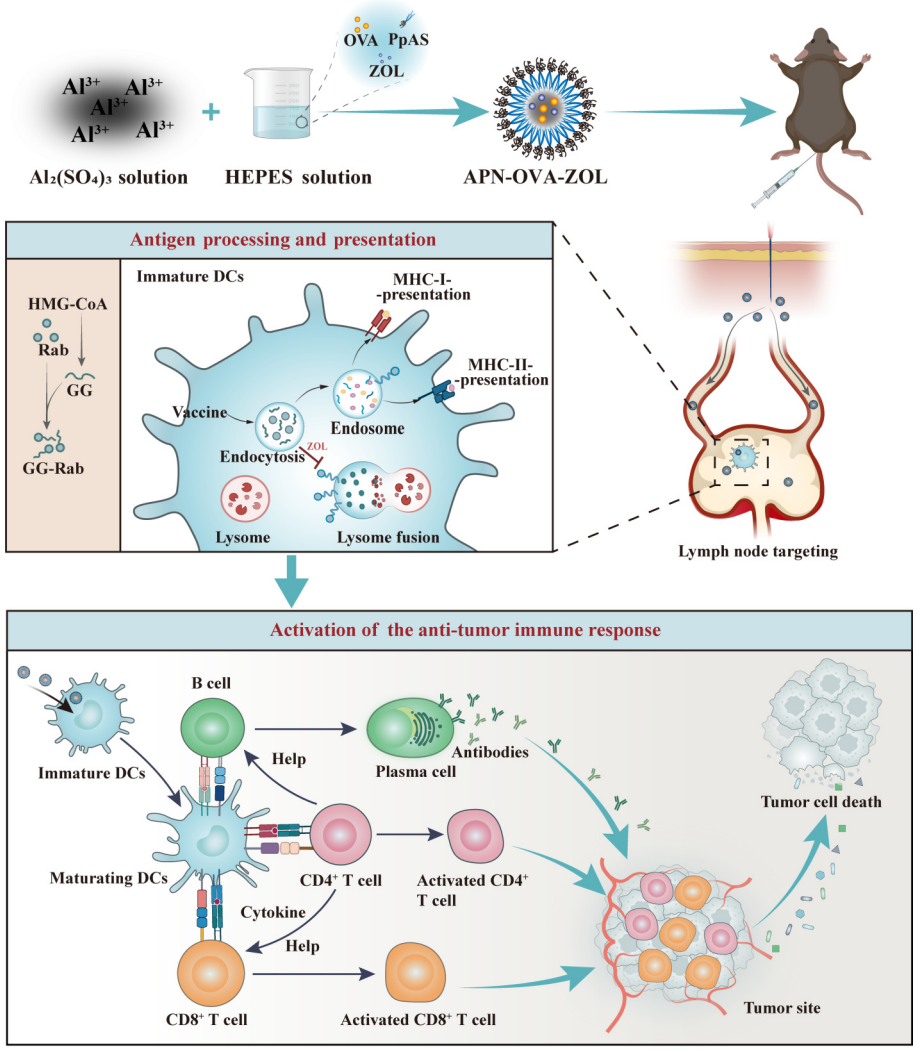

Figure 1 Schematic illustration of the fabrication process and working mechanisms of APN-OVA-ZOL. APN-OVA-ZOL was prepared by a simple two-phase mixing method. After subcutaneous vaccination, APN-OVA-ZOL can efficiently target lymph nodes and be taken up by lymph node-resident dendritic cells. Zoledronate in nanovaccine works by inhibiting the mevalonate pathway, which provided isoprene for the acrylation of different proteins (eg, the Rab superfamily), resulting in promoted antigen cross-presentation. As a result, APN-OVA-ZOL triggered a series of potent anticancer immune responses, which would robustly inhibit the growth of tumors and prolonged the survival of the tumor-bearing mice.

glycol (PEG) derivative (PEG_n-ploy(AGE-Suc)$_m$ (PpAS)) for preparing a nano-sized aluminum hydroxide-based nanovaccine (APNs). Model antigen ovalbumin (OVA) and ZOL as an immune stimulator were co-loaded onto the nanovaccines (APN-OVA-ZOL) using a facile mixing method. We showed that APN-OVA-ZOL displayed excellent antigen cross-presentation abilities, which led to striking levels of cellular immune responses. *In vivo*, APN-OVA-ZOL nanovaccines significantly inhibited the growth and prolonged mice survival in a EG7-OVA tumor-bearing model.

2 Experimental

2.1 Materials and reagents

PpAS was synthesized in our group. ZOL (purity > 97%) and 2-ethanesulfonic acid (HEPES) (purity > 98%) was purchased from J&K Scientific (Beijing, China). Albumin from chicken egg white (OVA) was purchased from Sigma-Aldrich (MO, USA), and the endotoxin in OVA was removed with Pierce High-Capacity Endotoxin Removal Spin Columns (Thermo Fisher Scientific). $Al_2(SO_4)_3$ (purity > 99%) was purchased from Macklin (Shanghai, China). Recombinant mouse granulocyte macrophage colony-stimulating factor (GM-CSF) was purchased from R&D Systems (Minneapolis, MN, USA). Cell counting kit-8 (CCK-8) was purchased from Beyotime (Shanghai, China). ELISA kits for mouse IL-4, IL-6, IL-12, and TNF-α were purchased from eBioscience (California, USA). All antibodies (CD11c, SIINFEKL/H-2Kb, CD80, CD86, F4/80, CD4, CD8, IL-4, IFN-γ, CD44 and CD62L) against cell surface markers for flow cytometry were purchased from eBioscience (California, USA). All the other chemicals used are of analytical grade, and Milli-Q water (18 megohm/cm; Millipore Co.) was used for the preparation of all solutions.

2.2 Cells and animals

Murine dendritic cells DC 2.4 were obtained from the cell bank at the Chinese Academy of Science (Shanghai, China). B3Z T cells and EG7-OVA cells were obtained from American Type Culture Collection (ATCC). All of these cells were cultured in complete RPMI-1640 supplemented with 10% fetal bovine serum (FBS) and 1% penicillin/streptomycin.

Healthy female C57BL/6J mice (6–8 weeks) were purchased from Chengdu Dossy Experimental Animals Co. Ltd (Sichuan, China). All animal experiments were approved by the Institutional Animal Care and Ethics Committee of Sichuan University.

2.3 Synthesis and characterization of PpAS

PpAS was synthesized through a two-step reaction established in our laboratory. Firstly, to obtain PEG_n-poly(AGE)$_m$, 10 g methoxypolyethylene glycol 5000 (CH_3OPEG_{5k}) in a 100 mL three-necked round bottom flask, and an oil pump was used to remove oxygen. Next, nitrogen was slowly filled into the flask, and 0.1 g NaH was added at 150 °C to activate the hydroxyl group, and the temperature was cooled slowly to 120 °C for 2 h. Subsequently, 8 mL allyl diglycidyl ether (AGE) was added dropwise into the flask and the mixtures were stirred for 24 h. Afterward, the hydrochloric acid solution was used to adjust the pH of the system to neutral to stop the reaction, and dichloromethane was added to fully dissolve the resultant product. After the dichloromethane was removed by a rotary evaporator, the product PEG_n-poly(AGE)$_m$ was precipitated in pre-cooled ether.

In the next step, 0.5 g PEG_n-ploy(AGE)$_m$ and 0.53 g dimercaptosuccinic acid were dissolved in a methanol solution containing 0.5% 2-hydroxy-4'-(2-hydroxyethoxy)-2-methylpropiophenone (Photoinitiator 2959), and the mixture was irradiated with UV at a wavelength of 365 nm for 30 min. Finally, unreacted materials were removed by dialysis for three days, and the purified PpAS was lyophilized and stored at 4 °C for further use. The obtained PpAS was analyzed with a ^{1}H NMR (400 MHz, D_2O).

2.4 Fabrication and characterization of APN-OVA-ZOL

To fabricate APN-OVA, $Al_2(SO_4)_3 \leftrightarrow 18H_2O$ (10 mM) was dissolved in ultrapure water (Phase A). PpAS (10 μL, 10 mg/mL) and OVA aqueous solutions (10 μL, 1 mg/mL) were added to 4-(2-hydroxyethyl) piperazine-1-ethanesulfonic acid (HEPES) (100 μL, 100 mM, pH 8.0) with gentle stirring (Phase B). Next, phase A was slowly added to phase B with strong mixing under a vortex shaker for 1 min at room temperature. As for the preparation of APN-OVA-ZOL, adding ZOL (12.5 μL, 10 mg/mL) to HEPES before mixing. To study the loading capacity of OVA and ZOL, APN-OVA-ZOL was purified by ultrafiltration, and amounts of OVA and ZOL in the filtrates were measured by using bicinchoninic acid (BCA) assay kit and high-performance liquid chromatography (HPLC), respectively.

The size and zeta potential of APN-OVA and APN-OVA-ZOL were measured by using a Nano Zetasizer (Malvern, Worcestershire, UK). The surface morphology of APN-OVA-ZOL was characterized by transmission electron microscopy (TEM, H-600, Hitachi, Japan). APN-OVA-ZOL was added onto copper grids and negatively stained. To investigate the stability of the formulations, the size and zeta potential of APN-OVA and APN-OVA-ZOL were measured every day for a week.

To further investigate the stability of aluminum salt nanovaccines, the size of APN-OVA and APN-OVA-ZOL in phosphate-buffered saline (PBS) solution (10% serum) were measured at 0, 12, and 24 h. At the same time, the absorbance of 600 nm of APN-OVA and APN-OVA-ZOL was measured under the condition of incubation with 10% serum at different time points, and the transmittance was calculated using the absorbance.

To further explore the storage stability of APN-OVA-ZOL under different conditions, the formulations were placed at 4 and 25 °C, and their particle sizes were measured weekly for two consecutive weeks.

2.5 *In vitro* release profiles of OVA and ZOL from APN-OVA-ZOL

To obtain AF594-labeled OVA (AF594-OVA), AF594 dye (0.88 mg) was added into OVA (10 mg) solution in carbonate solution (0.5 M, pH 9.5–9.6), which was stirred overnight at room temperature. Next, free AF594 dye was removed by dialysis, and the purified AF594-OVA was lyophilized and stored at 4 °C for further use. The release profiles of AF594-OVA and ZOL from APN-OVA-ZOL were studied at 37 °C in PB buffer (with a pH of 7.4 or 5.5) as the release medium. Briefly, freshly fabricated nanoparticles were placed in a dialysis bag. Subsequently, the dialysis bag was immersed in the release medium. At predetermined intervals, 500 μL of the release medium, present outside the dialysis bag, was withdrawn. The solution was replenished with the same volume of fresh release medium. The release amounts of AF594-OVA were measured using fluorescence spectroscopy (Ex. 580 nm, Em. 620 nm). The amounts of ZOL in the release medium were measured by HPLC.

2.6 *In vitro* cellular uptake

To obtain fluorescein isothiocyanate-labeled OVA (FITC-OVA), 10 mg of OVA was dissolved in a carbonate solution (0.5 M, pH 9.5–9.6). Next, 2.6 mg of fluorescein isothiocyanate was added to the OVA solution. The mixture was stirred at room temperature for 12 h. Next, free fluorescein isothiocyanate was removed by dialysis, and the purified FITC-OVA was lyophilized and stored at 4 °C for further use.

DC2.4 cell suspension (1×10^6 cells per well) was inoculated into 12-well plates and incubated with OVA, OVA+ZOL, APN-OVA, or APN-OVA-ZOL that contain 5 μg OVA and with or without 25 μg ZOL at 37 °C with 5% carbon dioxide for 1 or 3 h. Then, the cells were collected, centrifuged, and washed with PBS three times. Finally, the uptake of various formulations was analyzed by measuring the percentage of FITC-positive cells using flow cytometry (BD, USA).

To explore the uptake mechanisms of APN-OVA and APN-OVA-ZOL in DC2.4 cells, the cells were pretreated with various cell uptake inhibitors for 1 h. The following cell uptake inhibitors were used: dextran sulfate (100 μg/mL), chlorpromazine (20 μM), methyl-β-cyclodextrin (10 μM), nystatin (25 μM), and poly-l-lysine (200 μg/mL). Then, APN-OVA-ZOL containing 5 μg of FITC-OVA was added into the cells and incubated for another 1 h. After incubation, the cells were collected by centrifugation and washed three times with PBS, and the uptake of antigen was analyzed using flow cytometry.

2.7 Primary mouse bone marrow-derived dendritic cells (BMDCs) culturing and analysis

BMDCs were obtained from mouse bone marrow, as described previously [21]. In brief, the femur and tibia were carefully removed from 8-week-old male C57BL/6 mice. Bone marrow cells were washed several times using a 1 mL syringe with RPMI 1640 medium (Gibco, USA) supplemented with 10% heat-inactivated FBS (Gibco, USA), 1% penicillin-streptomycin liquid (Solarbio, Beijing, China), and 50 μM 2-mercaptoethanol, until the bone becomes completely devoid of bone marrow (the bone becomes white). Cell fragments and muscle tissue masses were removed by a 70 μm cell strainer, and the resulting marrow cells were then collected for centrifugation at 200 g for 10 min. Next, bone marrow cells were seeded at 2×10^7 cells per well bacteriological petri dishes in 10 mL of R10 containing GM-CSF (20 ng/mL), recorded as day 0. On day 3, 10 mL R10 containing GM-CSF (20 ng/mL) was added to the plate. On day 5, BMDCs were carefully collected and then incubated with sterile PBS containing 50% FBS at 37 °C for 30 min to remove residual granulocytes. The percentage of CD11c-positive cells was detected by BD flow cytometry to evaluate the purity of BMDC.

2.8 Geranylgeranyl diphosphate (GGPP) level *in vitro*

To measure the GGPP level *in vitro*, BMDCs were treated with PBS, OVA, OVA+ZOL, APN-OVA, and APN-OVA-ZOL that contain OVA (5 μg) and/or ZOL (25 μg) for 8 h. Then the cells were harvested and processed according to the manufacturer's instructions of Mouse GGPP assay kit (COIBO BIO, Shanghai, China) to detect the cellular GGPP level.

2.9 Evaluation of Rab5 expression by western blotting

To measure the expression of Rab5 in cell membrane and cytosol *in vitro*, BMDCs were incubated with PBS, OVA, OVA+ZOL, APN-OVA, and APN-OVA-ZOL that contain OVA (5 μg) and/or ZOL (25 μg) for 8 h. Then, the cells were collected to obtain membrane proteins and cytosol proteins according to the manufacturer's instructions of Membrane and Cytosol Protein Extraction Kit (Beyotime Biotechnology, Shanghai, China). The final protein concentration was determined using the BCA Protein Assay Kit (YEASEN, Shanghai, China) Western blotting was performed per standard methods. Antibodies for Rab5, Na^+/K^+-ATPase, and β-actin were purchased from HuaBio (Hangzhou, China). Secondary antibodies conjugated to horseradish peroxidase were used in conjunction with a chemiluminescent reagent to visualize protein bands.

2.10 *In vitro* assays of OVA cross-presentation and mechanisms studies

BMDCs were seeded at 1.5×10^6 cells per well in 12-well plates and incubated with OVA, OVA+ZOL, APN-OVA, or APN-OVA-ZOL that contain OVA (5 μg) and/or ZOL (25 μg) for 4 h. Then the cells were washed and incubated for another 20 h. Meanwhile, to explore the mechanism of APN-OVA-ZOL to promote cross-presentation, geranylgeraniol (GGOH, 50 μg)—a mevalonate pathway rescue agent was added into APN-OVA-ZOL formulation after 4 h of incubation. Afterward, cells were collected, washed twice with PBS, and stained with PE-conjugated anti-mouse SIINFEKL/H-2Kb antibody, and the cross-presentation was analyzed by flow cytometry.

To evaluate the activation effect of B3Z T cells by OVA cross-presenting, DC2.4 were seeded at 1×10^5 cells per well in 96-well plates and incubated with OVA, OVA+ZOL, APN-OVA or APN-OVA-ZOL that contain OVA (5 μg) and/or ZOL (25 μg) for 18 h. Meanwhile, to explore the mechanism of APN-OVA-ZOL to promote cross-presentation, GGOH—a mevalonate pathway rescue agent was added into APN-OVA-ZOL formulation after 4 h of incubation. Then the medium was replaced with fresh medium containing 2×10^5 B3Z T cells, and cultures were co-incubated for a further 22 h. Next, the co-cultured cells were washed with PBS, followed by incubation with 150 μL chlorophenol red β-D-garactopyranoside buffer (0.15 mM chlorophenol red β-D-garactopyranoside, 100 mM 2-mercaptoethanol, 0.2% TritonX-100 and 9 mM $MgCl_2$ in PBS) for 72 h at 37 °C. After the incubation, the absorbance at 570 nm of each well was measured using a Tecan Spark 10M multimode microplate reader (Switzerland).

To evaluate the activation effect of T cells by OVA cross-presenting, BMDCs were seeded at 1×10^6 cells per well in 12-well plates and incubated with OVA, OVA+ZOL, APN-OVA or APN-OVA-ZOL that contain OVA (5 μg) and/or ZOL (25 μg) for 18 h. Meanwhile, GGOH was added into APN-OVA-ZOL formulation after 4 h of incubation. Meanwhile, spleens were harvested from healthy mice and ground into single-cell suspension through a 70-μm cell sieve. Next, splenocytes were incubated with ammonium-chloride potassium (ACK) lysis buffer (0.15 M NH_4Cl, 0.01 M $KHCO_3$, 1 mM EDTA, pH 7.4) to remove the red cells. Then the BMDCs medium was replaced with fresh medium containing 1×10^6 spleen lymphocytes, and cultures were co-incubated for a further 48 h. After incubation, cells were stained with FITC-conjugated anti-mouse CD8 and APC-conjugated anti-mouse CD137, and analyzed using BD flow cytometry.

2.11 *In vitro* activation of BMDCs

BMDCs were seeded at 1.5×10^6 cells per well in 12-well plates and incubated for 24 h with OVA, OVA+ZOL, APN-OVA, or APN-OVA-ZOL that contain OVA (5 μg), and/or ZOL (25 μg). Cells

incubated with PBS served as a negative control. After washing twice with PBS, the cells were stained with FITC-conjugated anti-mouse CD80 antibody and APC-conjugated anti-mouse CD86 antibody (eBioscience, CA, USA). The expression of costimulatory molecules CD80 and CD86 on the surface of BMDCs was detected using flow cytometry.

Cytokines in BMDC culture supernatant including Interleukin 12 (IL-12), Interleukin 6 (IL-6), and Tumor necrosis factor alpha (TNF-α), were detected by using cytokine detection kits according to the manufacturer's protocol.

2.12 Lymph node distribution of APN-OVA-ZOL and activation of lymph node-resident DCs *in vivo*

To evaluated the biodistribution of different formulations, AF594-labeled OVA, APN-OVA, or APN-OVA-ZOL, each containing 10 μg OVA, were subcutaneously injected into the tail root of mice. Mice were sacrificed at 6 h post-injection, and tissues and organs including heart, lung, liver, spleen, kidney and were lymph node collected. The images of fluorescence were captured using the IVIS Spectrum *in vivo* Imaging System (CRi, USA) and analyzed with Living Image software (CRi, USA).

To obtain Cy5-labeled OVA (Cy5-OVA), Cy5 dye (1.38 mg) was added into OVA (20 mg) solution in carbonate solution (0.5 M, pH 9.5–9.6), which was stirred overnight at room temperature. Next, free Cy5 dye was removed by dialysis, and the purified Cy5-OVA was lyophilized and stored at 4 °C for further use. OVA, OVA+ZOL, APN-OVA, or APN-OVA-ZOL containing Cy5-OVA (5 μg) and/or ZOL (25 μg) were subcutaneously injected into the tail root of mice. The inguinal lymph nodes were surgically removed from the vaccinated mice at 2, 6, 12, 24, or 36 h. The lymph nodes were grinded to the single-cell suspension through a 70-μm cell sieve. Cells were washed twice with PBS, surface-stained with superbright 430-conjugated anti-mouse CD11c antibody and PE-conjugated anti-mouse F4/80, and analyzed using BD flow cytometer.

To explore the activation of lymph node-resident DCs, mice were sacrificed on day 3 post immunization to collect their inguinal draining lymph nodes. The lymph nodes were then passed through a 70-μm cell sieve to recover single-cell suspension. Single cell suspensions were stained with PE-conjugated anti-mouse SIINFEKL/H-2Kb antibody to analyze the DC cross-presentation *in vitro*.

2.13 Animal immunization and detection of immune responses

All of the mice were administered by tail root subcutaneous injection of various formulations, including OVA, OVA+ZOL, APN-OVA, or APN-OVA-ZOL. Each formulation contained 2 μg of OVA or 25 μg of ZOL. After primary immunization on day 0, booster immunizations were given on days 14 and 28. Mice were sacrificed on day 35, and blood samples and spleens were collected for analysis.

Blood samples were obtained from the angular vein on day 35, and serum was obtained by centrifugation for detection of antibody. Firstly, transplant plates (96-well) were coated with OVA (100 μL, 1.0 μg/well) in carbonate-bicarbonate buffer (0.1 M, pH 9.6) overnight at 4 °C. Secondly, the plates were washed three times with phosphate buffer containing 0.05% tween 20 (PBST) and incubated with PBS containing 1% bovine serum albumin (200 μL/well) at 37 °C for 2 h. Thirdly, the plates were washed five times with PBST and incubated at 37 °C for 1 h with horseradish peroxidase-conjugated anti-mouse IgG, IgG1 or IgG2a (diluted 1:10,000, 100 μL/well). Fourthly, after washing six times with PBST, the plates were incubated with trimethylboron (InnoReagents, China) (100 μL/well) at 37 °C for 10–20 min. Finally, the reaction was stopped by 1 M H_2SO_4 (50 μL/well), and the absorbance at 450 nm was measured using a Tecan Spark 10M multimode microplate reader (Switzerland).

For the intracellular cytokine staining of splenocytes, spleens were harvested from mice 7 days after the last immunization and ground into single-cell suspension through a 70-μm cell sieve. Then, splenocytes were incubated with ACK lysis buffer to remove the red cells. Next, splenocytes were incubated at 37 °C for 6 h with OVA (100 μg/mL), SIINFEKL (2 μg/mL) and brefeldin A (5 μg/mL). After incubation, cells were stained with APC-eFluor780-conjugated anti-mouse CD4, FITC-conjugated anti-mouse CD8, PE-conjugated anti-mouse IL-4, and APC-conjugated anti-mouse IFN-γ, and analyzed using BD flow cytometry.

For the detection of cytokines in the supernatant of spleen cell culture, splenocytes were incubated with OVA (100 μg/mL) and SIINFEKL (2 μg/mL) at 37 °C for 72 h. Then the supernatant was collected and cytokines, including Interleukin 4 (IL-4) and Tumor necrosis factor alpha (TNF-α) were detected by using cytokine detection kits according to the manufacturer's protocol.

For the detection of spleen cell proliferation, splenocytes were incubated with OVA (100 μg/mL) and SIINFEKL (2 μg/mL) at 37 °C for 72 h. Then Cell Counting Kit-8 solution (Dojindo, China) (10 μL) was added into each well and incubated with cells at 37 °C for another 4 h. The cell proliferation was determined by detecting absorbance at 450 nm using a Tecan Spark 10M multipurpose microplate reader (Tecan, Switzerland).

For the detection of memory T cells, splenocytes were incubated with OVA (100 μg/mL) and SIINFEKL (2 μg/mL) at 37 °C for 72 h. Then, the cells were collected and stained with APC-eFluor 780-conjugated anti-mouse CD4, APC-conjugated anti-mouse CD44, and PE-conjugated anti-mouse CD62L. The percentages of central memory T cells ($CD4^+CD44^+CD62L^+$ T cells and $CD8^+CD44^+CD62L^+$ T cells) were measured by using flow cytometry.

For the detection of cytokines in the supernatant of lymph nodes cell culture, lymphocytes were incubated with OVA (100 μg/mL) and SIINFEKL (2 μg/mL) at 37 °C for 72 h. Then the supernatant was collected and cytokines, including Interleukin 4 (IL-4), Interleukin 6 (IL-6), and Tumor necrosis factor alpha (TNF-α) were detected by using cytokine detection kits according to the manufacturer's protocol.

2.14 Tumor challenge

Mice were inoculated with 5×10^5 EG7-OVA cells on day 0 and randomly divided into five groups including PBS, OVA, OVA+ZOL, APN-OVA, and APN-OVA-ZOL (n = 8). They were vaccinated with different formulations subcutaneously at the root of the tail on days 3, 7, and 11. The length and width of the tumor were measured using a vernier caliper every 2 days and the tumor volumes were calculated as volume (mm^3) = length × $width^2$/2. The endpoint of measurement is reached when the tumor length is over 20 mm or tumor volume exceeds 2000 mm^3 or the tumor occurred ulceration.

2.15 Tumor microenvironment

To evaluate the efficacy of APN-OVA-ZOL in stimulating immune activation within the tumor microenvironment, female C57BL/6 mice were subcutaneously implanted with 1×10^6 EG7-OVA cells

on day 0. The mice then received subcutaneous injections at the base of the tail with various formulations, including PBS, OVA, OVA+ZOL, APN-OVA, or APN-OVA-ZOL on days 3, 7, and 11. Each formulation contained 2 μg OVA and with or without 25 μg ZOL. On Day 15, the tumor-bearing mice were euthanized, and tumors were harvested for further analysis. The harvested tumors were gently ground into single-cell suspension through a 70 μm cell sieve. The cancerous cells were treated with ACK lysis buffer to remove red blood cells, washed twice with PBS, and then resuspended in PBS supplemented with 2% FBS.

As for the evaluation of $CD8^+$ T cells immune response, 50 μL of diluted surface staining antibodies, including FITC-conjugated anti-mouse CD8 and PE-conjugated anti-mouse CD69 were added in each sample and incubated with the cells for 30 min at 4 °C. After washing twice with PBS, the cells were resuspended in 200 μL of intracellular fixation buffer and incubated for another 30 min at room temperature. The cells were then washed twice with permeabilization buffer and stained with 100 μL of diluted intracellular cytokines antibodies containing PE/Cy7-conjugated anti-mouse Granzyme B and APC-conjugated anti-mouse IFN-γ in the darkness for 30 min. Finally, after washing with PBS, flow cytometry was used for detection.

2.16 Safety evaluation

Mice were treated in the same regime as described in the animal immunization study. For blood routine testing, whole blood on day 35 was collected to detect the hematological indicators including white blood cell (WBC), platelet (PLT), monocytes (Mon), and lymphocyte (LYM) by using a standard blood analyzer.

2.17 Statistical analyses

All statistical analyses were performed with GraphPad Prism 8.0 (GraphPad Software). All results are expressed as mean ± standard error of mean (SEM). Statistical analysis of data was presented using t-test. Levels of significant differences were expressed as follows, $^*p < 0.05$; $^{**}p < 0.01$; $^{***}p < 0.001$; $^{****}p < 0.0001$.

3 Results and discussion

3.1 Fabrication and characterization of APN-OVA-ZOL

We prepared aluminum hydroxide-PpAS nanoparticles (APNs) by a simple vortex method using a wheat-like PEG derivative PpAS. The structure of PpAS was confirmed by ^{1}H NMR. According to the integrated area of PEG and the double bond peak of NMR hydrogen spectrum, the number of PEG repeat units can be calculated to be 113, AGE repeat units to be 12, and the molecular weight of the synthesized PpAS is further calculated as 7980 (Fig. S1 in the Electronic Supplementary Material (ESM)). As shown in Fig. 2(a), APN-OVA-ZOL was fabricated by first mixing PpAS with modal antigen ovalbumin (OVA) and ZOL dissolved in HEPES solution (pH = 8.0). $Al_2(SO_4)_3$ solution was slowly added to the above mixture with strong vortexing at room temperature for 1 min to form APN-OVA-ZOL. As the control, the preparation of APN-OVA is similar to the above, but without the addition of zoledronate. It was found that both APN-OVA and APN-OVA-ZOL were of similar size and ζ potential with a narrow size distribution. Transmission electron microscopy showed that APN-OVA and APN-OVA-ZOL were monodispersed and spherical in shape (Figs. 2(b) and 2(c)). The OVA encapsulation efficiency for APN-OVA and APN-OVA-ZOL was 66.37% ± 3.41% and 72.48% ± 4.30%, respectively. As revealed by the HPLC assay (Fig. S2 in the ESM), APN-OVA-ZOL achieved a high encapsulation efficiency of 87% for adjuvant ZOL (Fig. 2(c)). The hydrodynamic diameters of those nanoparticles in 4 °C showed no significant variation within one week, indicating the good storage stability of those nanoparticles (Fig. 2(d)). Interestingly, we found that the bisphosphonate group in ZOL can interact with aluminum through coordination, further increasing the stability of aluminum salt nanoparticles. As shown in Fig. 2(e) and Fig. S3 in the ESM, the size of APN-OVA increased by about 100 nm after 12 h and approached about 300 nm after 24 h in PBS buffer, whereas such a change was not found for APN-OVA-ZOL. To better simulate the *in vivo* physiological environment, we measured the transmittance of different formulations at different time points in the presence of 10% serum. The transmittance of the APN-OVA decreased significantly from 90.50% ± 0.10% to 61.87% ± 2.90% over time (Fig. S4 in the ESM), indicating a certain degree of aggregation after the incubation of APN-OVA with serum Only a slight decrease of transmittance was detected for APN-OVA-ZOL group until the endpoint of 24 h. Additionally, to evaluate the stability of the APN-OVA-ZOL at different temperatures, we used dynamic light scattering to continuously monitor changes in particle size. Over a two-week period, we observed stable particle size and PDI values, when the samples were stored at 4 or 25 °C (Fig. 2(f)).

As shown in Fig. S5 in the ESM, the APN-OVA-ZOL formulation released only about 25% of OVA at pH 7.4 over 28 h, whereas at pH 5.5, approximately 60% of OVA was released. Similarly, at pH 7.4, only 25% of ZOL was released within 35 h, whereas about 70% was released at pH 5.5. These findings suggested that the nanoparticles remain stable in physiological conditions and promote the release of antigen and adjuvant in the acidic environment of the endosome. Notably, compared to the release profile of OVA at pH 5.5, the release of ZOL was relatively slower within the first 10 hours but accelerated between 10 to 28 h, reaching up to 70% release. This phenomenon may be attributed to ZOL's coordination exchange interactions with the aluminum hydroxide core being tighter compared to OVA's electrostatic interactions with the same.

3.2 Cellular uptake, cross-presentation properties, and maturation of antigen-presenting cells *in vitro*

To assess the internalization efficiency of various formulations in DC2.4 cells, OVA, OVA+ZOL, APN-OVA, or APN-OVA-ZOL that contain FITC-OVA (5 μg) and/or ZOL (25 μg) were incubated with DC2.4 cells for 1 or 3 h. As shown in Fig. 3(a), the encapsulation of OVA in APNs significantly increased the internalization of OVA by 3–4 times. Interestingly, the uptake efficiency of APN-OVA-ZOL at 1 h was lower than that of APN-OVA, possibly because ZOL affected the isoprene modification of Rab GTPase, a key protein in vesicular transport [22]. When the ingestion time was extended to 3 h, the effect of ZOL in delaying endocytosis was alleviated and the ingestion efficiency was comparable to that of APN-OVA. Slow internalization has indeed previously been shown to favor cross-presentation in DCs [23]. Conceivably, the maximum stability of the antigen can be achieved when the antigen is continuously but more slowly absorbed into the early endosome. The antigen in the early endosomes provides a continuous release pool of antigen that might be used over extended periods for the continuous formation of peptide-MHC class I complexes (Fig. 3(b)). To further explore the internalization mechanism of APN-OVA-ZOL, DC2.4 cells were pretreated with

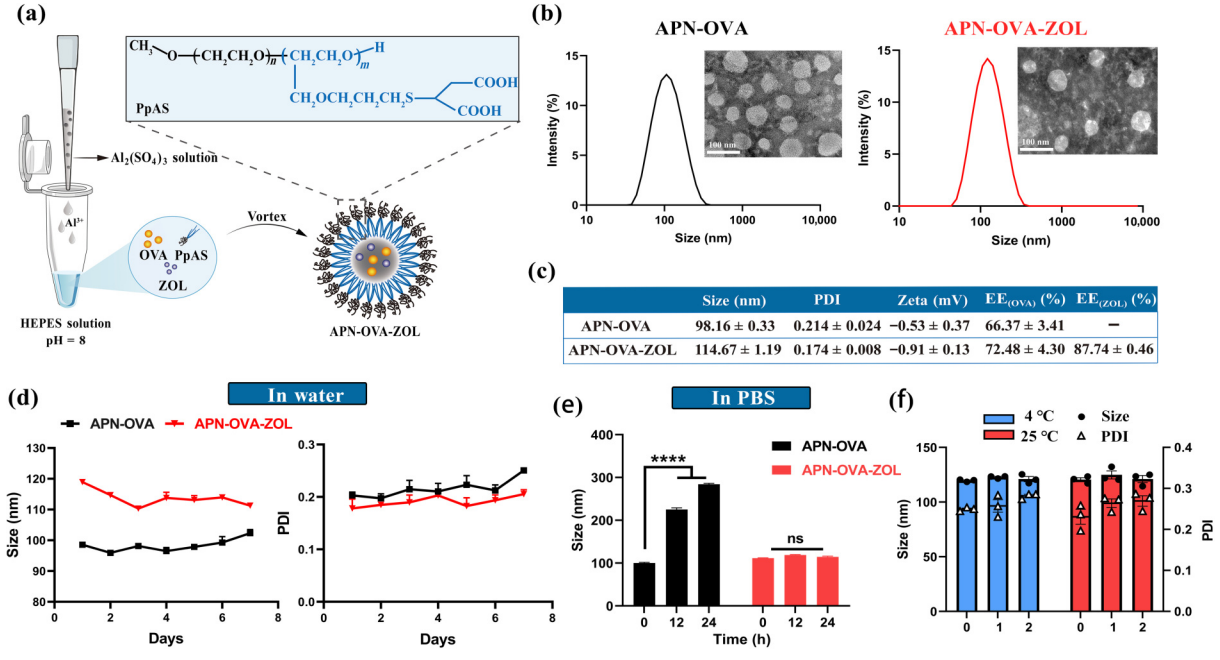

	Size (nm)	PDI	Zeta (mV)	$EE_{(OVA)}$ (%)	$EE_{(ZOL)}$ (%)
APN-OVA	98.16 ± 0.33	0.214 ± 0.024	−0.53 ± 0.37	66.37 ± 3.41	–
APN-OVA-ZOL	114.67 ± 1.19	0.174 ± 0.008	−0.91 ± 0.13	72.48 ± 4.30	87.74 ± 0.46

Figure 2 Characterization of APN-OVA-ZOL. (a) Chemical structures of PEG derivative PpAS and preparation process of APN-OVA-ZOL. (b) Hydrodynamic size and transmission electron micrographs of APN-OVA and APN-OVA-ZOL. Scale bar: 100 nm. (c) OVA encapsulation efficiency (EE, %) of APN-OVA and APN-OVA-ZOL, and ZOL encapsulation efficiency (EE, %) of APN-OVA-ZOL. (d) Changes in particle size (nm) and polydispersity index (PDI) of APN-OVA and APN-OVA-ZOL incubated at 4 °C for one week. (e) The size distribution of APN-OVA and APN-OVA-ZOL in 1 × PBS solution at room temperature was detected with dynamic light scattering at 0, 12, and 24 h. (f) Changes in particle size and PDI of APN-OVA-ZOL at different temperature over two weeks. Data are represented as mean ± SEM (n = 3). $^*p < 0.05$; $^{**}p < 0.01$; $^{***}p < 0.001$, $^{****}p < 0.0001$.

different inhibitors to block specific endocytic pathways. The results showed that the internalization of APN-OVA-ZOL was reduced by about 80% when cells were incubated at 4 °C, suggesting that the uptake of APN-OVA-ZOL was energy dependent (Fig. 3(c)). Meanwhile, chlorpromazine and dextran sulfate also significantly inhibited the internalization of APN-OVA-ZOL, indicating that clathrin and scavenger receptor-mediated endocytic pathways were mainly involved in the internalization of APN-OVA-ZOL [24–26]. The uptake pathway of APN-OVA was consistent with that of APN-OVA-ZOL (Fig. S6 in the ESM), which was mediated by energy, clathrin, and scavenger receptors, indicating that the absorption pathway of aluminum salt nanovaccines was not changed by the addition of ZOL.

The mevalonate pathway regulates the geranylacylation modification of Rab GTPases, which facilitates the localization of Rab GTPases in membranous organelles such as endosomal lysosomes and endoplasmic reticulum, and realizes substance transfer and signal transmission [27]. In antigen-presenting cells (APC), pathogens internalized by phagocytosis are first degraded in phagosomes and endosomes, and then degraded antigens bound to specific membrane receptors are transported to the cell surface through vesicles transport. Thus, inhibiting the mevalonate pathway could serve as a strategy to reduce antigen degradation and drive adaptive immune response, helping to slow dendritic cell acidification and phagosomal maturation to promote cross-presentation and trigger a robust T-cell immune response [28]. To determine the regulatory effect of intervention in the MVA pathway on antigen processing pathways in BMDCs, we performed a bottom-up study. GGPP is a major metabolite of the MVA pathway and a key protein required for post-translational geranylgeranylation of Rab5.

We first detected the GGPP level in BMDCs with different treatments. As displayed in Fig. 3(d), compared to APN-OVA, OVA+ZOL, and OVA, APN-OVA-ZOL remarkably decreased the GGPP level of BMDCs, which was attributed to that ZOL inhibited the farnesyl pyrophosphate synthase (FPPS) of MVA pathway to reduce GGPP production. We further evaluated the distribution of Rab5 in BMDCs by western blot. As shown in Fig. S7 in the ESM, APN-OVA-ZOL reduced the amount of Rab5 localized to membranes and elevated the amount in the cytosol, thereby delaying endosomal antigens enter into degradative lysosomes.

We next quantified the efficiency of cross-presentation by detecting the formation of the OVA257-264 peptide (SIINFEKL)-MHC-I complex on the BMDC surface [29]. The results demonstrated that APN-OVA-ZOL NPs could remarkably enhance the proportion of 25d1.16-positive cells, achieving much higher levels of cross-presentation than APN-OVA, OVA + ZOL, and OVA alone (Fig. 3(e)). In addition, we sought to investigate whether the increased antigen cross-presentation would result in improved B3Z T cell activation. DC2.4 cells were pulsed for 18 hours with the different formulations and subsequently incubated with B3Z cells for 22 h. Antigen-dependent T cell activation was measured via a colorimetric assay [30]. As expected, incubation of DCs with APN-OVA-ZOL led to significantly enhanced activation of B3Z T cells, which was about 1.43-fold and 1.96-fold over APN-OVA and OVA+ZOL, respectively (Fig. 3(f)). Moreover, APN-OVA-ZOL supplementation with GGOH did not increase cross-presentation and T cell activation. To further investigate the specific activation of cellular immunity by APN-OVA-ZOL through antigen cross-presentation, we co-incubated BMDCs treated with various formulations with spleen lymphocytes. As shown in Fig. 3(g), APN-OVA-ZOL induced the highest level of $CD8^+$ T cell activation (CD137), surpassing that of other experimental groups. Additionally, the supplementation of GGOH mitigated the inhibition of the mevalonate pathway by ZOL, leading to reduced $CD8^+$ T cell activation, aligns with the

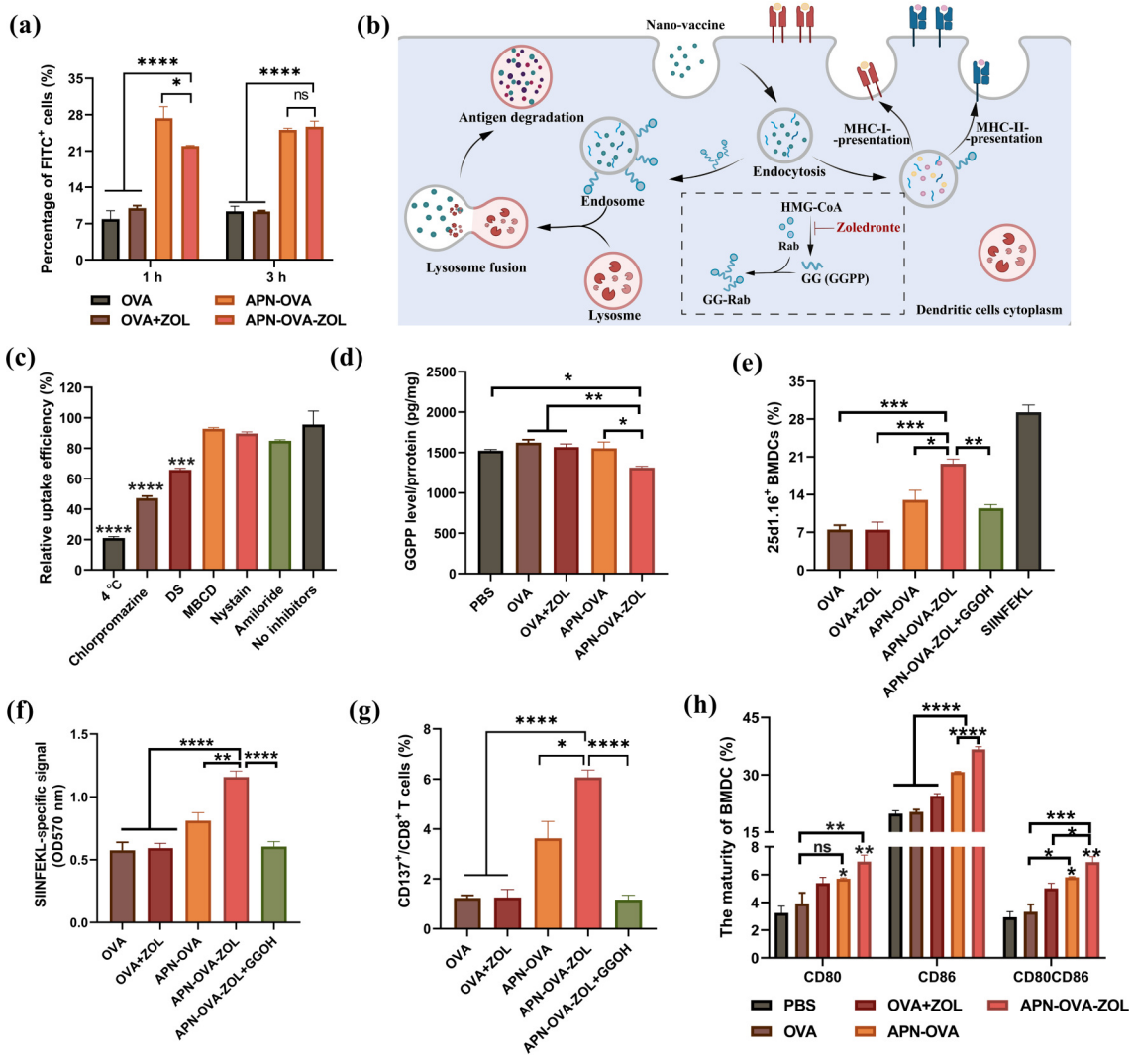

Figure 3 Cellular uptake, antigen cross-presentation, and maturity of APN-OVA-ZOL *in vitro*. (a) OVA, OVA+ZOL, APN-OVA, and APN-OVA-ZOL internalization by DC2.4 cells. DC2.4 cells were incubated with formulations for 1 and 3 h before analysis by flow cytometry. (b) Schematic of the adjuvanticity of zoledronate for antigen preservation and presentation. (c) Screening of potential mechanisms of APN-OVA-ZOL internalization by DC2.4 cells. (d) The GGPP level in BMDCs with different treatments. (e) Cross-presentation of OVA in BMDCs. (f) MHC class I presentation of different formulations by DCs was analyzed by measuring the activation of B3Z hybridoma $CD8^+$ T cell line upon 22 h incubation with DCs pulsed for 18 h with titrated amounts of the indicated formulations. (g) Percentages of $CD137^+$ cells in $CD8^+$ T cells were measured by flow cytometry. (h) Percentages of cells that upregulated $CD80^+$ and $CD86^+$ after overnight incubation with titrated amounts of the indicated formulations. Data are represented as mean ± SEM (n = 3–4). $^*p < 0.05$; $^{**}p < 0.01$; $^{***}p < 0.001$, $^{****}p < 0.0001$.

findings observed in B3Z T cells. These results highlight the positive role of mevalonate pathway inhibition in enhancing cross-presentation and T cell activation [31].

In addition to class I antigen presentation by DCs, generating a robust $CD8^+$ T cell response also requires engagement of costimulatory molecules and cytokine signaling, which provide context to T cell initiation and enhancement of T cell activation and effector function [32, 33]. Flow cytometer assays were carried out to analyze the expression of CD80 and CD86 on DC surface after various treatments for 24 h. Results showed that APN-OVA-ZOL could trigger the strongest DC maturation, as shown by the highest level of $CD80^+$, $CD86^+$, and $CD80^+CD86^+$ cells (Fig. 3(g)). Using the conditioned media from our *in vitro* activation of DCs assay, we further examined the secreted cytokine under the various treatment conditions. As shown in Fig. S8 in the ESM, cells treated with APN-OVA-ZOL induced elevated secretion of IL-6, TNF-α, and IL-12p70 secretion when compared to other groups. These results together suggested that the encapsulation of OVA and ZOL in APNs robustly enhanced DC internalization and remarkably enhance the cross-presentation properties and maturation of formulations *in vitro*.

3.3 Targeting lymph nodes and effective activation of lymph node-resident DCs by APN-OVA-ZOL

To further study the LN-targeting capability of formulations and explore its antigen processing patterns in LNs, we dissected the inguinal LNs (ILNs) of mice at various experimental time points after the tail base injection of different formulations and ground the LNs for flow cytometry analysis. As shown in Figs. 4(a) and 4(b), a large percentage of DCs and macrophages displayed the uptake of OVA within a short time (2–6 h) after the APN-OVA or APN-OVA-ZOL were injected, whereas only very small amounts of OVA in free-OVA group were taken up by antigen-presenting cells in lymph nodes within 2–6 h. The percentage of DCs and

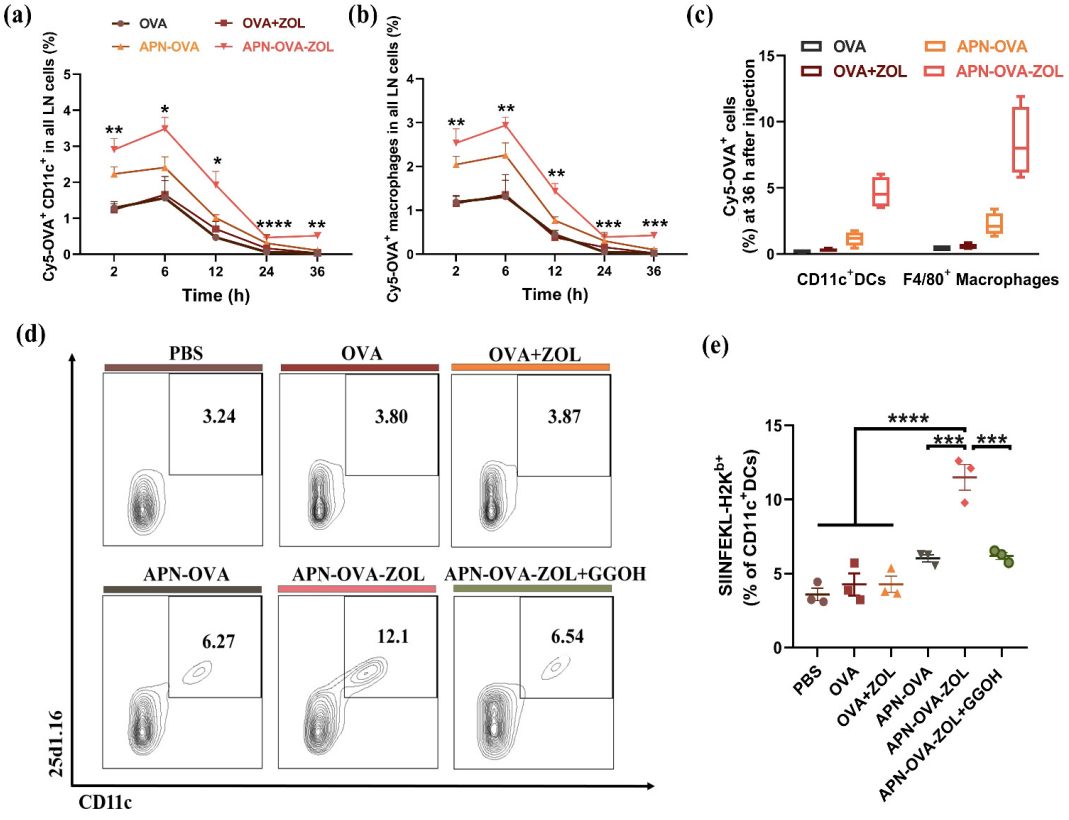

Figure 4 The draining lymph node targeting ability and the activation of lymph node–resident DCs by APN-OVA-ZOL. (a) and (b) Mice were subcutaneously immunized at the tail root with OVA, OVA+ZOL, APN-OVA,or APN-OVA-ZOL (5 μg Cy5-OVA); then inguinal lymph nodes were isolated at the indicated times. Percentages of Cy5-OVA$^+$ cells (a) in CD11c$^+$ DCs or (b) in F4/80$^+$ macrophages cells were measured by flow cytometry. (c) Percentages of Cy5-OVA$^+$ cells in CD11c$^+$ DCs or in F4/80$^+$ macrophages cells were measured by flow cytometry after subcutaneous administration at the tail root for 36 h. (d) Representative flow cytometry data and (e) statistic data to show OVA antigen cross-presentation efficiencies induced by different formulations of NPs *in vivo*. Data are represented as mean ± SEM (n = 3–4). *p < 0.05; **p < 0.01; ***p < 0.001, ****p < 0.0001.

macrophages that uptook OVA in OVA and OVA+ZOL groups decreased significantly after 6h. In contrast, APN-OVA-ZOL group showed much higher levels of antigen retention in lymph nodes in the following hours. For instance, at 36 h, the proportion of DC and macrophage that uptake OVA in lymph nodes was 4.92 times and 4.25 times of APN-OVA group, respectively (Fig. 4(c)). The differential antigen processing in lymph nodes observed is likely due to zoledronate inhibit the geranylgeranylation of small GTPases, resulting in arrested endosomal maturation, prolonged antigen retention.

Then, we carried out the biodistribution analysis of OVA, APN-OVA, and APN-OVA-ZOL in major organs (heart, liver, spleen, lungs, and kidneys) and lymph nodes using an *in vivo* imaging system (IVIS) 6 h post subcutaneous injection into the tail base of mice. As expected, no fluorescence signals were identified in major organs. The delivery of APN-OVA-ZOL demonstrated the highest intensity in the lymph nodes (Fig. S9 in the ESM).

We then investigated the promotion effect of APN-based nanovaccine on the antigen cross-presentation *in vivo*. Mice were sacrificed on day 3 post immunization to collect their inguinal draining lymph nodes to analyze the percentage of CD11c$^+$SIINFEKL$^+$ DCs. Notably, treatment with APN-OVA-ZOL showed the highest level of CD11c$^+$SIINFEKL-H2Kb$^+$ antigen cross-presented DCs in the draining lymph nodes. Similarly, when we used mevalerate pathway rescue agent—GGOH to explore the mechanism behind, APN-OVA-ZOL supplementation with GGOH did not induce more abundant MHC-peptide complexes on the cell surface. These results were consistent with the observation that the addition of GGOH leads to decreased cross-presentation properties *in vitro* (Figs. 4(d) and 4(e)). Therefore, our results demonstrated that APN-OVA-ZOL nanovaccine can inhibit the MVA pathway that is required for geranylgeranylation of small GTPases in DCs, resulting in arrested endosomal maturation. As a result, APN-OVA-ZOL prolonged antigen retention, promoted antigen presentation, and further induced a powerful T-cell immune response.

3.4 Ability of APN-OVA-ZOL to activate immune responses

Antibodies bind specifically to antigens, activate the body's immune defense mechanism, and play a role in eliminating the antigen [34]. To study the capacity of APN-OVA-CpG to elicit humoral responses, C57BL/6J mice were immunized with various formulations: PBS, OVA, OVA+ZOL, APN-OVA, or APN-OVA-ZOL, on days 0, 14, and 28. Blood was sampled on day 35 to study the antibodies against OVA. The antibody results showed that APN-OVA-ZOL elicited higher total IgG titers compared to all other preparations (Fig. 5(a)). Furthermore, APN-OVA-ZOL elicited the highest heterotypic IgG1 titers, which were 1.23-fold higher than that of APN-OVA or OVA+ZOL (Fig. 5(b)). Furthermore, APN-OVA-ZOL also elicited significantly enhanced the IgG2a titer as compared to APN-OVA and OVA+ZOL (Fig. 5(c)).

As Th1-associated responses and Th2-associated responses are likely attributed to the help of CD4$^+$ T cells, we next investigated

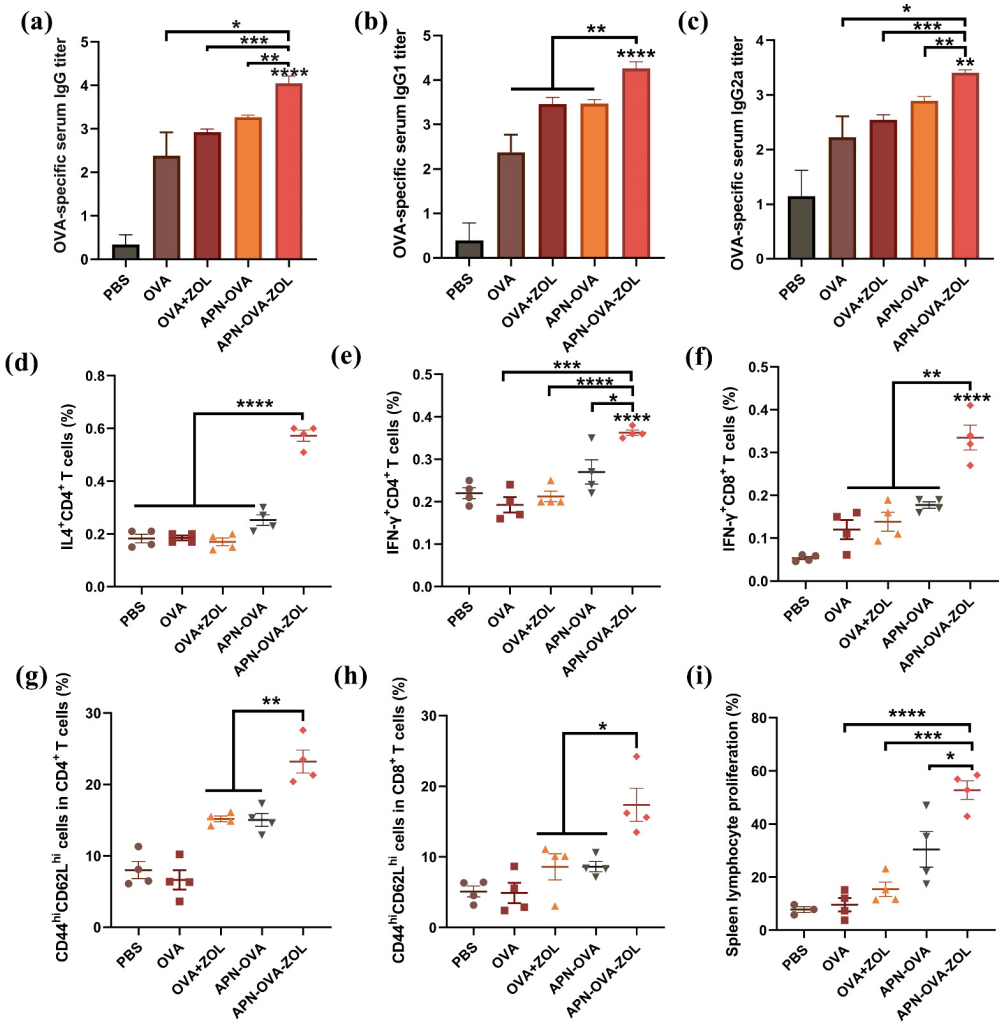

Figure 5 Ability of APN-OVA-ZOL to activate immune responses. Serum from vaccinated mice was collected, and antigen-specific titers of day 35, (a) IgG, (b) IgG1, and (c) IgG2a were measured using ELISA kits. Percentages of (d) IL-4$^+$CD4$^+$ T cells, (e) IFN-γ$^+$CD4$^+$ T cells, and (f) IFN-γ$^+$CD8$^+$ T cells were determined using flow cytometry. Percentages of (g) CD4$^+$CD44$^+$CD62L$^+$ T cells and (h) CD8$^+$CD44$^+$CD62L$^+$ T cells (central memory T cells, TCM) in the spleen were measured using flow cytometry. (i) Splenocyte proliferation rates were determined using CCK-8 kits. Data are represented as mean ± SEM (n = 3–4). *p < 0.05; **p < 0.01; ***p < 0.001, ****p < 0.0001.

OVA-specific CD4$^+$ T cell responses elicited by different vaccine formulations [35]. CD4$^+$ T cell responses were determined by studying the percentage of IL4$^+$CD4$^+$ T cells and IFN-γ$^+$CD4$^+$ T cells after restimulating harvested splenocytes with OVA antigens on day 35. Our results showed that APN-OVA-ZOL-inoculated group showed the highest frequency of IL4$^+$CD4$^+$ T cells and IFN-γ$^+$CD4$^+$ T cells (Figs. 5(d) and 5(e)).

We next evaluated CD8$^+$ T cell-mediated immunity, which plays a critical role in conferring protection against cancerous cells. Following stimulating splenocytes with ovalbumin peptide SIINFEKL (H-2Kb) and intracellular IFN-γ-staining, only the APN-OVA-ZOL-nanoparticles-immunized mice significantly stimulated the production of IFN-γ-CD8$^+$ T cells (Fig. 5(f)), indicating aluminum salt nanoparticles co-loaded with OVA and ZOL nanoparticles were superior in inducing cytotoxic CD8$^+$ T cells than the control formulations. Similarly, higher levels of IL-4 and TNF-α were also detected in splenocytes culture medium in APN-OVA-ZOL group (Fig. S10 in the ESM). And APN-OVA-ZOL induced higher levels of IL-4, IL-6, and TNF-α secretion in lymphocytes culture medium (Fig. S11 in the ESM). Moreover, T cells with the central memory phenotype (CD44$^+$CD62L$^+$) were also significantly elevated in the splenocytes of APN-OVA-ZOL-immunized mice (Figs. 5(g) and 5(h), and Fig. S12 in the ESM). Therefore, we speculated that APN-OVA-ZOL could induce powerful immune memory and provide long-term protection for the body. We further determined splenocyte proliferation, mice immunized with APN-OVA-ZOL exhibited obvious splenocyte proliferation as compared to the control nanoparticles (Fig. 5(i)). To assess *in vivo* safety of APN-OVA-ZOL nano-vaccine, the hematological indicators of mice including white blood cell (WBC), platelet (PLT), monocytes (Mon), lymphocyte (Lymph) were detected on seven days after the last immunization. There was no significant change in all hematological indicators (WBC, PLT, Mon, and LYM) in mice after being treated with OVA, OVA+ZOL, APN-OVA-ZOL, and APN-OVA-ZOL, indicating good safety *in vivo* (Fig. S13 in the ESM). All these above results evidenced the ability of APN-OVA-ZOL has the ability to induce a full spectrum of immune responses, with Th1 coverage and cytolytic T cell responses being highly sought after in cancer vaccine development.

3.5 APN-OVA-ZOL dramatically enhanced anti-tumor efficacy

We next investigated the potential use of APN-OVA-ZOL in therapeutic vaccinations against tumors. In order to evaluate antigen-specific responses, a EG7 subline that has been engineered to express the full-length ovalbumin model antigen (EG7-OVA cells) was used as tumor challenge. In this study, female C57BL/6 mice were inoculated subcutaneously in the right posterior side with 5×10^5 EG7-OVA cells on day 0, and then immunized with one of five treatments (PBS, OVA, OVA+ZOL, APN-OVA, or APN-OVA-ZOL) on days 3, 7 and 11 (Fig. 6(a)). Notably, APN-OVA-ZOL vaccination showed significantly slower tumor growth compared with APN-OVA or free OVA+ZOL-immunized mice (Fig. 6(b)). The ability of the various formulations to slow tumor growth was directly proportional to their ability to prolong survival. APN-OVA-ZOL-immunized mice significantly the median lifespan to 41 days (Fig. 6(c)). This very encouraging result also showed that the effector $CD8^+$ T cells induced by aluminum salt nanoparticles coadministration of OVA and ZOL were indeed capable of recognizing and killing their antigen-bearing target cell *in vivo*.

Then, we investigated the immune activation capacity of our formulations in tumors, focusing on $CD8^+$ T cell immune response, which play crucial roles in the killing of cancerous cells [36]. We found that the APN-OVA-ZOL treatment group had the highest level of $CD8^+$ T cells activation (CD69) in tumors (Fig. 6(d)). Meanwhile, the proportion of IFN-γ^+ $CD8^+$ T cells increased to approximately 0.82% following APN-OVA-ZOL administration, significantly higher than that in the PBS (0.38%), OVA (0.48%), OVA+ZOL (0.52%) and APN-OVA (0.45%) groups (Fig. 6(e)). Furthermore, mice treated with APN-OVA-ZOL demonstrated a

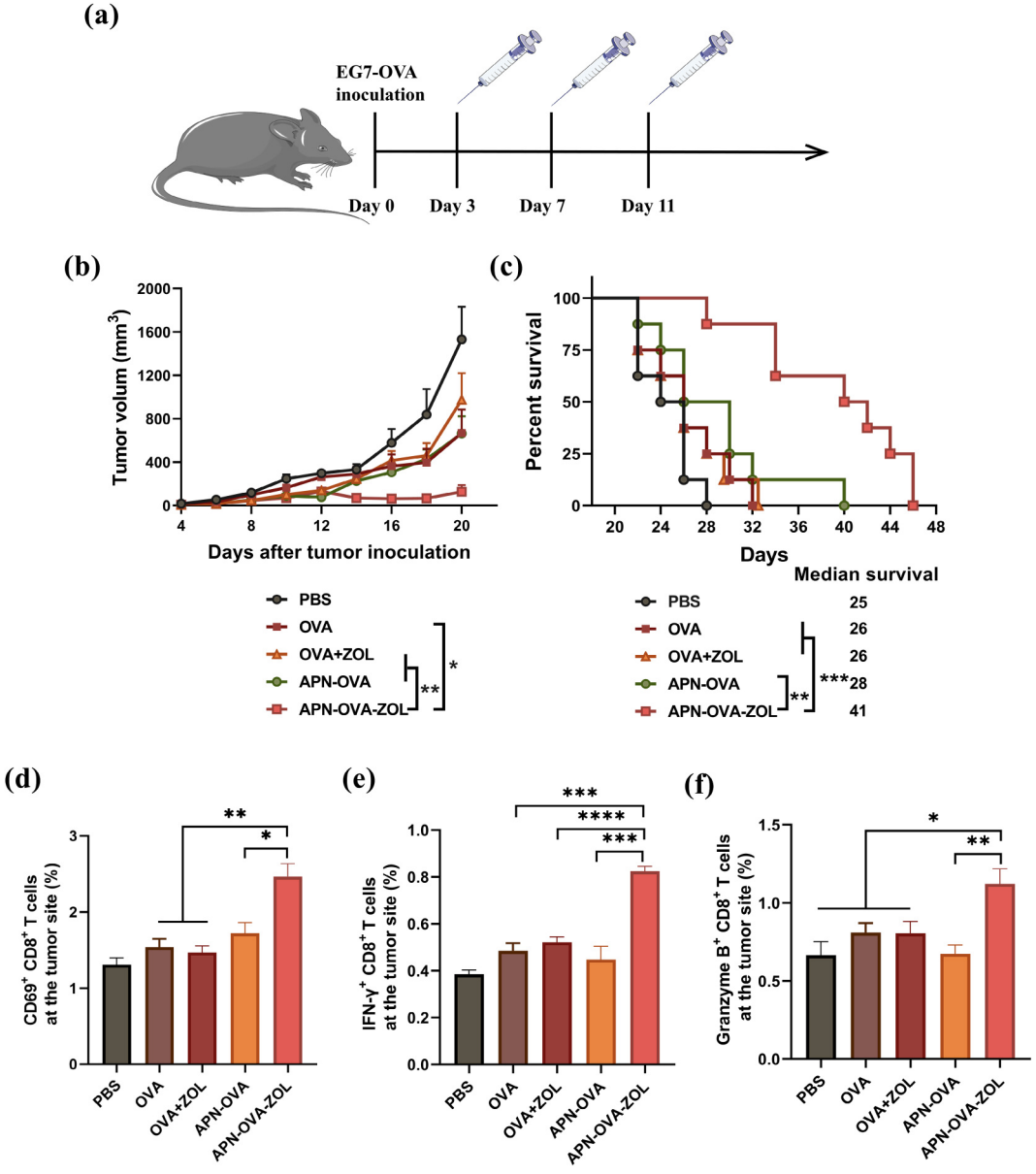

Figure 6 Tumor growth inhibition potency of APN-OVA-ZOL and survival curve of mice. (a) Schematic illustration to show the therapeutic tumor models experiment design. (b) Tumor growth curves and (c) Kaplan-Meier survival curves of mice immunized with PBS, OVA, OVA+ZOL, APN-OVA and APN-OVA-ZOL (n = 8). Percentages of (d) $CD69^+CD8^+$ T cells, (e) IFN-γ^+ $CD8^+$ T cells, and (f) $GranzymeB^+CD8^+$ T cells at the tumor sites were measured using flow cytometry (n = 4). Data are represented as mean ± SEM. *$p < 0.05$; **$p < 0.01$; ***$p < 0.001$, ****$p < 0.0001$.

greater proportion of Granzyme B^+ $CD8^+$ T cells in tumors, which was 1.69, 1.38, 1.40 and 1.66 times higher than that of the PBS, OVA, OVA+ZOL and APN-OVA groups, respectively (Fig. 6(f)). Overall, the above results demonstrated that APN-OVA-ZOL effectively induced $CD8^+$ T cell activation and elevated cytotoxic $CD8^+$ T cell production at the tumor sites, thus significantly improving anti-tumor efficacy.

4 Conclusion

This versatile nanovaccines platform displayed several advantages as follows. This work provided a rational target for vaccine adjuvant, namely the MVA pathway, for regulating antigen transport process in DC to augment immunotherapy efficiency. Besides, the system repurposed FDA-approved drugs including Alum and ZOL, which promising to be an extremely promising approach to addressing cancer treatment needs. Moreover, nano-engineering of classical aluminum adjuvants could achieve potent antitumor immune responses due to the effective LNs-targeted delivery of ZOL and intrinsic immunostimulatory activities. In conclusion, the combinatorial nanovaccines, APN-OVA-ZOL, successfully interfered in endosomal antigens transportation of DCs, thereby boosting DC-mediated immunotherapy. Overall, we demonstrated a promising and powerful adjuvant strategy for design a versatile nanovaccines to amplify cellular immune response. Our work suggested that regulating the antigen-processing process of antigen-presenting cells could be a promising strategy to construct effective nanovaccines for cancer immunotherapy. Clearly, our work also offered a powerful illustration that this strategy should be explored very widely in the fabrication of other types of important vaccines (e.g. vaccines against viral infections) in which antigen cross-presentation is an essential process.

Electronic Supplementary Material: Supplementary material (synthetic and chemical structures of PpAS, quantification of ZOL in formulation, stability of the formulation, cellular uptake inhibition, western blot anaysis of Rab protein, secretion levels in cell culture medium, representative profiles of flow cytometry analysis, safety evaluation) is available in the online version of this article at https://doi.org/10.26599/NR.2025.94907010.

Data availability

All data needed to supportthe conclusions in the paper are presented in the manuscript and the Electronic Supplementary Material. Additional data related to this paper may be requested from the corresponding author upon request.

Acknowledgements

This work was supported by the National Natural Science Foundation of China (Nos. 82320108020 and 81925036), the National Key Research and Development Program of China (No. 2023YFC2307700), 111 project (No. B18035), and the Fundamental Research Funds for the Central Universities

Declaration of competing interest

All the contributing authors report no conflict of interests in this work.

Author contribution statement

C. T. H.: Data curation, validation, writing manuscript, experimental design. P. H. H.: Data curation, writing manuscript, experimental design. X. T.: Validation, experimental design. S. T. B.: Validation, experimental design. M. Q.: Validation, experimental design. Y. T. Z.: Validation, experimental design. Z. F. G.: Validation, experimental design. G. S. D.: Project administration, writing manuscript. X. S.: Project administration, funding acquisition, writing manuscript. All the authors have approved the final manuscript.

Informed consent

Not applicable.

Ethics statement

The animal experiments were carried out following the guidelines of the Care and Use of Laboratory Animals of Sichuan University Ethics Committee and were approved by the Committee on the Ethics of Animal Experiments of Sichuan University (license no.: SYXK (Chuan) 2023-0113).

Use of AI statement

None.

References

[1] Shi, S. T.; Zhu, H. R.; Xia, X. Y.; Liang, Z. H.; Ma, X. H.; Sun, B. B. Vaccine adjuvants: Understanding the structure and mechanism of adjuvanticity. *Vaccine* **2019**, *37*, 3167–3178.

[2] Firdaus, F. Z.; Skwarczynski, M.; Toth, I. Developments in vaccine adjuvants. In *Vaccine Design: Methods and Protocols, Volume 3. Resources for Vaccine Development*. Thomas, S., Ed.; Springer: New York, 2022; pp 145–178.

[3] Bonam, S. R.; Partidos, C. D.; Halmuthur, S. K. M.; Muller, S. An overview of novel adjuvants designed for improving vaccine efficacy. *Trends Pharmacol. Sci.* **2017**, *38*, 771–793.

[4] Hollingsworth, R. E.; Jansen, K. Turning the corner on therapeutic cancer vaccines. *npj Vaccines* **2019**, *4*, 7.

[5] Mempel, T. R.; Henrickson, S. E.; Von Andrian, U. H. T-cell priming by dendritic cells in lymph nodes occurs in three distinct phases. *Nature* **2004**, *427*, 154–159.

[6] Le Gall, C. M.; Weiden, J.; Eggermont, L. J.; Figdor, C. G. Dendritic cells in cancer immunotherapy. *Nat. Mater.* **2018**, *17*, 474–475.

[7] Jiang, H.; Wang, Q.; Sun, X. Lymph node targeting strategies to improve vaccination efficacy. *J. Control. Release* **2017**, *267*, 47–56.

[8] Chen, Y.; De Koker, S.; De Geest, B. G. Engineering strategies for lymph node targeted immune activation. *Acc. Chem. Res.* **2020**, *53*, 2055–2067.

[9] Joffre, O. P.; Segura, E.; Savina, A.; Amigorena, S. Cross-presentation by dendritic cells. *Nat. Rev. Immunol.* **2012**, *12*, 557–569.

[10] Agallou, M.; Margaroni, M.; Tsanaktsidou, E.; Badounas, F.; Kammona, O.; Kiparissides, C.; Karagouni, E. A liposomal vaccine promotes strong adaptive immune responses via dendritic cell activation in draining lymph nodes. *J. Control. Release* **2023**, *356*, 386–401.

[11] K. M.; MacParland, S. A.; Ma, X. Z.; Spetzler, V. N.; Echeverri, J.; Ouyang, B.; Fadel, S. M.; Sykes, E. A.; Goldaracena, N.; Kaths, J. M. et al. Mechanism of hard-nanomaterial clearance by the liver. *Nat. Mater.* **2016**, *15*, 1212–1221.

[12] Yang, Y. S. S.; Atukorale, P. U.; Moynihan, K. D.; Bekdemir, A.;

Rakhra, K.; Tang, L.; Stellacci, F.; Irvine, D. J. High-throughput quantitation of inorganic nanoparticle biodistribution at the single-cell level using mass cytometry. *Nat. Commun.* **2017**, *8*, 14069.

[13] Tseng, Y. C.; Xu, Z. H.; Guley, K.; Yuan, H.; Huang, L. Lipid-calcium phosphate nanoparticles for delivery to the lymphatic system and SPECT/CT imaging of lymph node metastases. *Biomaterials* **2014**, *35*, 4688–4698.

[14] Bai, S. T.; Jiang, H.; Song, Y. S.; Zhu, Y. N.; Qin, M.; He, C. T.; Du, G. S.; Sun, X. Aluminum nanoparticles deliver a dual-epitope peptide for enhanced anti-tumor immunotherapy. *J. Control. Release* **2022**, *344*, 134–146.

[15] Jiang, H.; Wang, Q.; Li, L.; Zeng, Q.; Li, H. M.; Gong, T.; Zhang, Z. R.; Sun, X. Turning the old adjuvant from gel to nanoparticles to amplify $CD8^+$ T cell responses. *Adv. Sci.* **2018**, *5*, 1700426.

[16] Bode, C.; Zhao, G.; Steinhagen, F.; Kinjo, T.; Klinman, D. M. CpG DNA as a vaccine adjuvant. *Expert Rev. Vac.* **2011**, *10*, 499–511.

[17] Zhang, Z. K.; Kuo, J. C. T.; Yao, S. Y.; Zhang, C.; Khan, H.; Lee, R. J. CpG oligodeoxynucleotides for anticancer monotherapy from preclinical stages to clinical trials. *Pharmaceutics* **2022**, *14*, 73.

[18] Prashar, A.; Schnettger, L.; Bernard, E. M.; Gutierrez, M. G. Rab GTPases in immunity and inflammation. *Front. Cell. Infect. Microbiol.* **2017**, *7*, 435.

[19] Xia, Y.; Xie, Y. H.; Yu, Z. S.; Xiao, H. Y.; Jiang, G. M.; Zhou, X. Y.; Yang, Y. Y.; Li, X.; Zhao, M.; Li, L. P. et al. The mevalonate pathway is a druggable target for vaccine adjuvant discovery. *Cell* **2018**, *175*, 1059–1073.e21.

[20] Zhang, Y. T.; Jiang, M.; Du, G. S.; Zhong, X. F.; He, C. T.; Qin, M.; Hou, Y. Y.; Liu, R.; Sun, X. An antigen self-assembled and dendritic cell-targeted nanovaccine for enhanced immunity against cancer. *Acta Pharm. Sin. B* **2023**, *13*, 3518–3534.

[21] Inaba, K.; Inaba, M.; Romani, N.; Aya, H.; Deguchi, M.; Ikehara, S.; Muramatsu, S.; Steinman, R. M. Generation of large numbers of dendritic cells from mouse bone marrow cultures supplemented with granulocyte/macrophage colony-stimulating factor. *J. Exp. Med.* **1992**, *176*, 1693–1702.

[22] Stenmark, H. Rab GTPases as coordinators of vesicle traffic. *Nat. Rev. Mol. Cell Biol.* **2009**, *10*, 513–525.

[23] A.; Kotsias, F.; Pauwels, A. M.; Carpier, J. M.; Jouve, M.; Timmerman, E.; Pace, L.; Vargas, P.; Maurin, M.; Gehrmann, U. et al. Toll-like receptor 4 engagement on dendritic cells restrains phago-lysosome fusion and promotes cross-presentation of antigens. *Immunity* **2015**, *43*, 1087–1100.

[24] Mettlen, M.; Chen, P. H.; Srinivasan, S.; Danuser, G.; Schmid, S. L. Regulation of clathrin-mediated endocytosis. *Annu. Rev. Biochem.* **2018**, *87*, 871–896.

[25] Tsubamotoa, Y.; Yamada, N.; Watanabe, Y.; Inaba, T.; Shiomi, M.; Shimano, H.; Gotoda, T.; Harada, K.; Shimada, M.; Ohsuga, J. I. et al. Dextran sulfate, a competitive inhibitor for scavenger receptor, prevents the progression of atherosclerosis in Watanabe heritable hyperlipidemic rabbits. *Atherosclerosis* **1994**, *106*, 43–50.

[26] Eguchi, S.; Takefuji, M.; Sakaguchi, T.; Ishihama, S.; Mori, Y.; Tsuda, T.; Takikawa, T.; Yoshida, T.; Ohashi, K.; Shimizu, Y. et al. Cardiomyocytes capture stem cell-derived, anti-apoptotic microRNA-214 via clathrin-mediated endocytosis in acute myocardial infarction. *J. Biol. Chem.* **2019**, *294*, 11665–11674.

[27] Jurczyluk, J.; Munoz, M. A.; Skinner, O. P.; Chai, R. C.; Ali, N.; Palendira, U.; Quinn, J. M. W.; Preston, A.; Tangye, S. G.; Brown, A. J. et al. Mevalonate kinase deficiency leads to decreased prenylation of Rab GTPases. *Immunol. Cell Biol.* **2016**, *94*, 994–999.

[28] Flannagan, R. S.; Jaumouillé, V.; Grinstein, S. The cell biology of phagocytosis. *Annu. Rev. Pathol.: Mech. Dis.* **2012**, *7*, 61–98.

[29] Granados, D. P.; Tanguay, P. L.; Hardy, M. P.; Caron, É.; De Verteuil, D.; Meloche, S.; Perreault, C. ER stress affects processing of MHC class I-associated peptides. *BMC Immunol.* **2009**, *10*, 10.

[30] Miura, N.; Akita, H.; Tateshita, N.; Nakamura, T.; Harashima, H. Modifying antigen-encapsulating liposomes with KALA facilitates MHC class I antigen presentation and enhances anti-tumor effects. *Mol. Ther.* **2017**, *25*, 1003–1013.

[31] Wingren, A. G.; Parra, E.; Varga, M.; Kalland, T.; Sjogren, H. O.; Hedlund, G.; Dohlsten, M. T cell activation pathways: B7, LFA-3, and ICAM-1 shape unique T cell profiles. *Crit. Rev. Immunol.* **2017**, *37*, 463–481.

[32] Schmitt, N.; Ueno, H. Regulation of human helper T cell subset differentiation by cytokines. *Curr. Opin. Immunol.* **2015**, *34*, 130–136.

[33] Tsai, L. M.; Yu, D. Follicular helper T-cell memory: Establishing new frontiers during antibody response. *Immunol. Cell Biol.* **2014**, *92*, 57–63.

[34] , T.; Sester, M. Detection of antigen-specific T cells based on intracellular cytokine staining using flow-cytometry. In *Virus-Host Interactions: Methods and Protocols*. Bailer, S. M.; Lieber, D., Eds.; Humana Press: Totowa, 2013; pp 267–274.

[35] Mosmann, T. R.; Coffman, R. L. TH1 and TH2 cells: Different patterns of lymphokine secretion lead to different functional properties. *Annu. Rev. Immunol.* **1989**, *7*, 145–173.

[36] Reina-Campos, M.; Scharping, N. E.; Goldrath, A. W. $CD8^+$ T cell metabolism in infection and cancer. *Nat. Rev. Immunol.* **2021**, *21*, 718–738.